Elucidating the Structure of Ethanol-Producing Active Sites at Oxide-Derived Cu Electrocatalysts

Oriol Piqué, Francesc Viñes, Francesc Illas, and Federico Calle-Vallejo*

Departament de Ciència de Materials i Química Física & Institut de Química Teòrica i Computacional (IQTCUB), Universitat de Barcelona, Martí i Franquès 1, 08028 Barcelona, Spain.

*Email: f.calle.vallejo@ub.edu

Abstract

The discovery of oxide-derived copper catalysts for CO_2 electroreduction is an outstanding advance in the field of electrocatalysis. Their low overpotentials and improved selectivity towards C_2 products make them unique. However, the structure of the active sites responsible for these improvements remains unclear. Herein, by means of a computational model including thermodynamic, kinetic, solvent and cation effects, we outline the atomic structure of the active sites responsible for ethanol evolution in OD-Cu catalysts. We also point out the specific features that determine selectivity and pinpoint the design criteria that should be fulfilled to enhance the catalysts' selectivity toward ethanol. Specifically, we propose that square, four-atom Cu islands are the active sites of OD-Cu for CORR to ethanol, as they display favorable *CO dimerization and ethanol selectivity by virtue of their square, undercoordinated structure.

Keywords: CO and CO_2 electroreduction, ethanol production, oxide-derived Cu, electrocatalysis, selectivity.

Introduction

In recent years, the electroreduction of CO_2 (CO_2RR) to high-value fuels for energy storage and environmental mitigation has received great attention and experienced pronounced advances.[1-4] Whereas numerous electrocatalysts are able to reduce CO_2 to CO, further reduction of CO (CORR) is needed to produce "electrofuels". Pioneering studies by Hori and coworkers showed that Cu is the most active metal towards CO_2RR and CORR to valuable commodities and fuels such as methane, ethylene, acetaldehyde, ethanol, and other minor products.[5-7] In spite of the great insight and important advances, some issues still hinder a large-scale implementation of CO_2 electrolyzers, namely large overpotentials and copper's low selectivity and faradaic efficiency.

Among the strategies devised to address those challenges, we highlight the redox treatments of metal electrodes.[3,8,9] In particular, oxide-derived Cu (OD-Cu) catalysts display relatively low overpotentials (< 0.4 V) and enhanced selectivity towards C_2 products, with ethanol appearing in substantial quantities,[10,11] compared to regular Cu catalysts. In spite of the significant enhancement and clear synthesis routes, the structure of the active sites at OD-Cu remains elusive. Some authors have proposed that such sites are located at grain boundaries.[11,12] According to them, engineering the grain boundaries by altering the oxide reduction method or modifying the synthesis procedure could yield catalysts with higher selectivity and activity towards multi-carbon products. Moreover, by using different kinds of OD-Cu catalysts, they show that high CORR activity on OD-Cu is concomitant to surface sites that bind CO more strongly than low-index and stepped Cu facets.[12]

Other authors have proposed that the presence of subsurface oxygen (O_{sb}) is the reason behind the noteworthy catalytic properties of OD-Cu.[13-15] Their works suggest that O_{sb} increases the CO binding energy to Cu surfaces. They argue that larger CO surface coverage results in more frequent C-C coupling, hence promoting the formation of C_2 products. However, recent computational and experimental works on the matter concluded that the stability of O_{sb} in OD-Cu catalysts is insufficient for it to stay at the subsurface under reaction conditions. It was also claimed that if O_{sb} were indeed present, it would have a negligible effect on CORR.[16-18] Instead, the results support the idea that the activity and selectivity improvements of OD-Cu versus metallic Cu are due to undercoordinated sites at rough surfaces, i.e. grain boundaries.

Since an atomic-scale understanding of OD-Cu catalysts remains elusive, we aim in this work at providing insights into the structure of their ethanol-producing sites.

Specifically, we propose that the active sites are square-symmetry four-atom islands sitting on neighboring fourfold hollow sites of Cu(100) facets (hereon denoted 4AD@Cu(100), where AD stands for Cu adatoms). This is justified by the following observations: (I) it has been shown experimentally and computationally that square sites promote C-C coupling.[19,20] (II) Cu(100) features square sites and is selective to ethylene,[20,21] whereas OD-Cu catalysts have enhanced ethanol selectivity.[11] (III) The active sites on OD-Cu bind CO more strongly than terraces and typical step-edge sites and their number grows alongside the amount of grain boundaries.[12] (IV) Acetaldehyde reduction to ethanol is enhanced at undercoordinated sites,[22] and acetaldehyde is an intermediate of CO reduction to ethanol on Cu catalysts.[21,23] (V) Experiments suggest that ethanol and ethylene are produced on different active sites on OD-Cu.[24]

For completeness, we supplemented the study with a non-square island (4AD@Cu(111)) and two common flat terraces (Cu(111) and Cu(100)). Our calculations indicate that 4AD@Cu(100) fulfills all the requirements set in I-V, as apart from being square and undercoordinated, it binds CO more strongly than terraces and step-edge sites and, more importantly, is selective to ethanol.

Computational Details

The density functional theory (DFT) simulations were performed using the Vienna ab initio simulation package (VASP)[25] with the Perdew-Burke-Ernzerhof (PBE) exchange-correlation functional,[26] known to be among the best functionals for the description of transition metal systems.[27] In addition, we used the projector augmented-wave method[28] to describe the effect of the inner cores on the valence electron density. The Cu(100) surfaces and the 4AD@Cu(100) model site were represented by a $(4\sqrt{2}\times4\sqrt{2})R45°$ supercell slab including 32 atoms per layer, while for Cu(111) and 4AD@Cu(111) (a four-atom island sitting on four neighboring fcc sites on Cu(111)) a $p(4\times4)$ supercell including 16 atoms per layer was used. Cu(211) was modeled as 3×1 supercell. These large supercells avoid lateral interactions between atom islands, adsorbates, and cations. All slab models were composed of four metal layers and modeled with the converged PBE lattice constant of Cu, namely 3.64 Å. The topmost two layers, the Cu islands and the adsorbates were relaxed in all directions, while the bottommost two layers were fixed at the bulk equilibrium distances to provide an adequate bulk environment to the surface region. On average, around ten different initial geometries for each adsorbate on

each active site were optimized, including monodentate, bidentate, and tridentate structures, when possible. A plane-wave cutoff of 450 eV was used and the Fermi level was smeared following the Methfessel-Paxton approach[29] with k_BT = 0.2 eV to facilitate convergence, always extrapolating the total energies to 0 K. The conjugate-gradient optimization scheme was used to search for the minimum-energy structures with iterations carried out until the maximal force on any atom was below 0.05 eV·Å^{-1}. Monkhorst-Pack meshes of 2×2×1 for Cu(100) and 4AD@Cu(100) were used to carry out the numerical integration in the reciprocal space, while for Cu(111) and 4AD@Cu(111) we used 3×3×1 meshes, which ensured convergence of adsorption energies within 0.05 eV. For Cu(211) a 4×5×1 mesh was used. The distance between repeated images in the vertical direction was larger than 13 Å and dipole corrections were applied. Isolated molecules were calculated in boxes of 9 Å × 10 Å × 11 Å using Gaussian smearing with k_BT = 0.001 eV, with further extrapolation to 0 K and considering the Γ point only. Transition-state geometries were found using the climbing-image nudged elastic band method,[30] ensuring that only one imaginary frequency along the reaction coordinate was obtained at the saddle point. The potential-dependent barriers were approximated as described in section S8.

The reaction free energies were approximated as $\Delta G \approx \Delta E_{DFT} + \Delta ZPE - T\Delta S + \Delta E_{solvation}$, where ΔE_{DFT} is the DFT-calculated reaction energy, ΔZPE is the zero-point energy change between reactants and products, $T\Delta S$ is the corresponding entropy change at 298.15 K, and $\Delta E_{solvation}$ is a solvation correction to the free energy. ZPE and TS_{vib} values were obtained from vibrational frequency calculations within the harmonic approximation. ΔS includes only the vibrational entropy for adsorbates and all contributions for free molecules. TS values of the free molecules were extracted from thermodynamic tables.[31] Solvation contributions to the free energies ($\Delta E_{solvation}$) were modelled as an external correction depending on the chemical nature of the adsorbates. Specific values calculated in previous works are given in Table S3 in the Supporting Information (SI).[21,32] For a brief summary on the assessment and use of such ad hoc solvation corrections, we refer the reader to ref. 33.

Considering previous reports on OD-Cu,[13,14,15] we performed a number of calculations including subsurface oxygen on 4AD@Cu(100) and 4AD@Cu(111). Most optimizations resulted in distorted slabs and/or the oxygen atom at the surface.

The computational hydrogen electrode was used to model proton-electron pairs.[34] Cation effects were modelled by explicit inclusion of a K atom on top of the slabs. Its most stable position was found by evaluating different possible sites around the adsorbate, see section S6. Although we calculated CO coupling barriers, we did not compute proton−electron transfer barriers, since, as noted recently by Rossmeisl et *al.*,[35] there is "not (yet) a method to obtain electrochemical barriers between realistic states at constant electrochemical conditions". Furthermore, we stress that Brønsted-Evans-Polanyi (BEP) relations exist for reactions where C, H, and O-containing species are involved.[36,37] Thus, we assume that kinetics and thermodynamics are well correlated for the reaction steps considered in this work.

Further computational details appear in the SI (Sections S1 to S3), and all the adsorption energies and corrections are reported in Section S4. Electrochemical stability considerations for 4AD@Cu(111) and 4AD@Cu(100) are provided in section S5. The coordinates of all the optimized systems appear in Section S9 and the corresponding images appear in Figures S1-S4.

Results and Discussion

We computed the thermodynamics of each proton-electron transfer of the CORR to C_2 products for the four different slab models described in the Computational Details section and shown in Figure 1a. Cu(100) was selected in view of the known ability of its square sites to catalyze C-C coupling.[3,19,21,38-41] 4AD@Cu(100) features favorable C-C coupling energetics in view of its square symmetry, and presumably enhanced ethanol selectivity by virtue of its undercoordination.[20,22] Thermodynamically, Cu(111) is the most stable facet of Cu and is probably abundant in polycrystalline Cu and OD-Cu. We note, however, that Cu(111) is not ostensibly active for the production of C_2 species,[3,20,38] and its selectivity is inclined towards methane. 4AD@Cu(111) is included to show that hexagonal-symmetry defects increase Cu(111)'s activity for C_2 production but are less active for C-C coupling than square facets. The analysis in section S5 suggests that 4AD@Cu(100) and 4AD@Cu(111) are stable under CORR conditions. We modeled the reaction pathway in Figure 1b,[21,39] which is known to comply with several key experimental observations.[3,40] However, we note that some other pathways have been proposed in the literature,[42-45] and we analyze some of them in section S7. We conclude that, at this level of theory, the pathway in Figure 1b is thermodynamically more favorable.

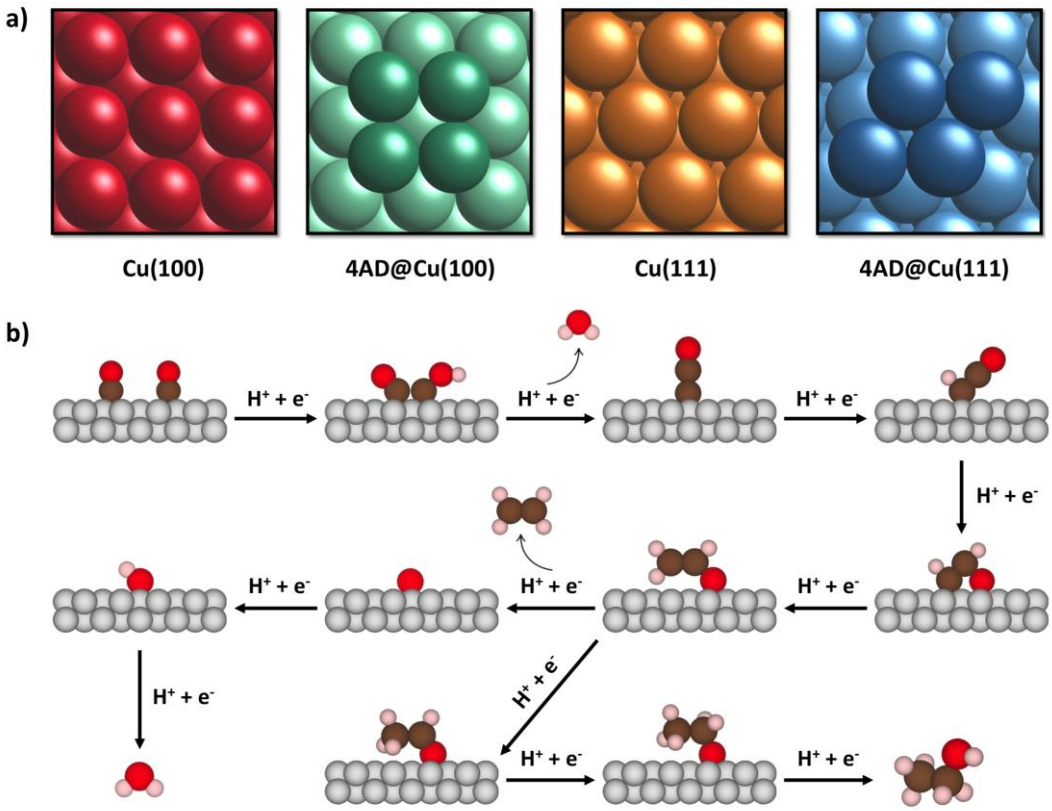

Figure 1. a) Schematics of the four different surface models used in this work. Cu(100), 4AD@Cu(100), Cu(111), and 4AD@Cu(111) surfaces are provided in red, green, orange, and blue, respectively. Island atoms are shown in darker colors. b) Reaction pathway for CORR to C_2 species. We depicted Cu, C, O, and H atoms as grey, brown, red, and pink spheres, respectively. Figures S1-S4 contain the optimized, minimum-energy geometries for each intermediate on each active site.

Previous studies have shown that alkaline cations affect the product selectivity of the CORR.[40,46,47] Thus, we included solvent and cation effects in our calculations to obtain a more realistic picture of the active sites. In the following, only the most stable situation for each adsorbate is considered, either solvated, with cations, or both in some specific cases (see Table S3 and section S5). Figure 2 shows the results in two separate free-energy diagrams: panel (a) contains the data for Cu(100) and 4AD@Cu(100), and panel (b) contains the data for Cu(111) and 4AD@Cu(111).

In these diagrams, the advance of the reaction can be followed for each of the four surface models and each one is depicted with a specific color. As also seen in Figure 1b, the reaction pathway bifurcates at the sixth proton-electron transfer, where one path leads to ethylene and the other to ethanol. This branching is represented in the diagrams by introducing a lighter version of each color that indicates the respective ethanol pathway. Similarly, the formula of each intermediate is depicted on the upper

part of Figure 2, where black corresponds to ethylene-pathway intermediates and grey to ethanol-pathway intermediates.

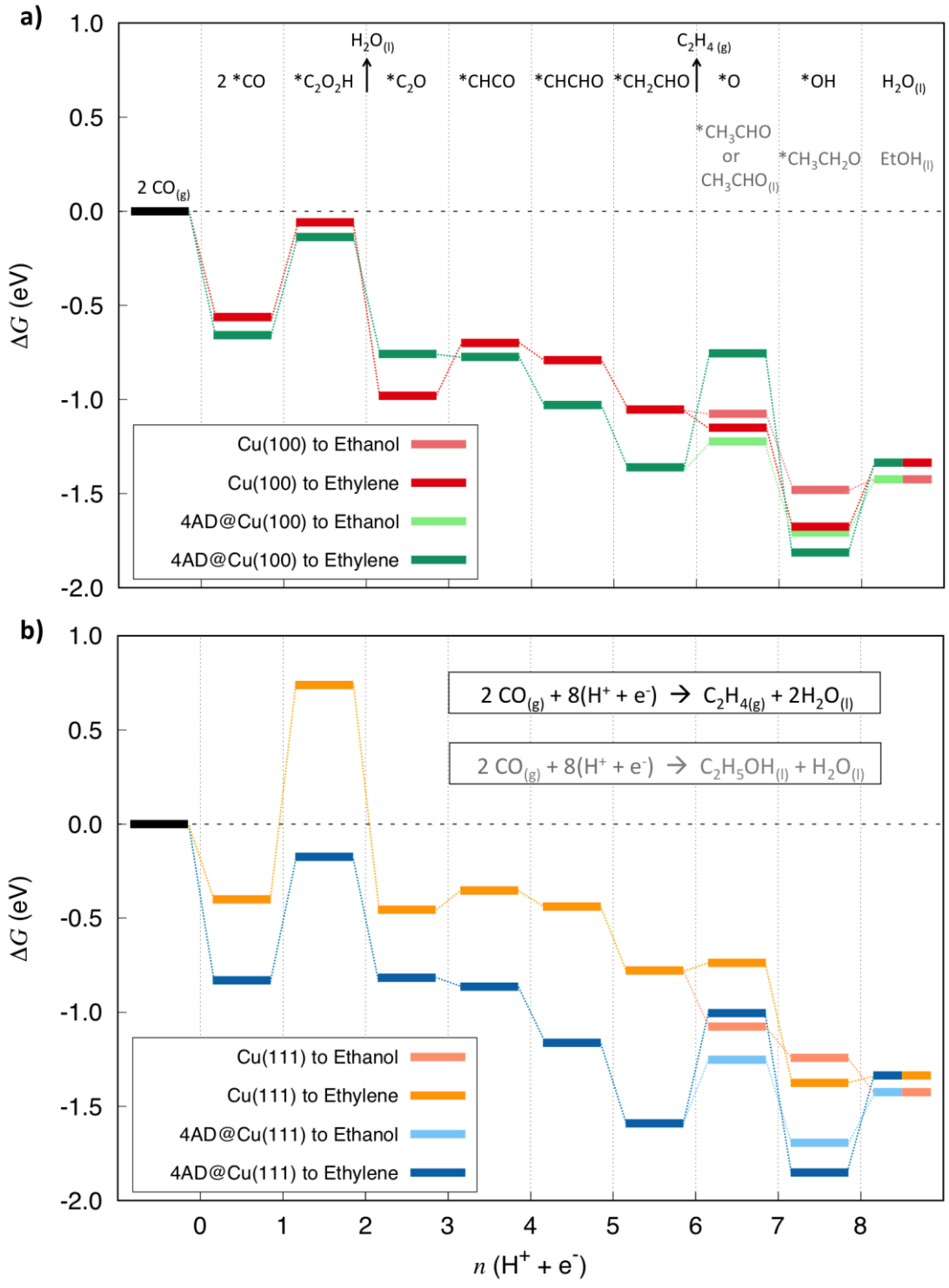

Figure 2. Free-energy diagrams including solvent and cation effects for all intermediates of the reactions on all four surfaces studied at 0 V vs RHE. a) Cu(100) (red) and 4AD@Cu(100) (green). b) Cu(111) (orange) and 4AD@Cu(111) (blue). The same colors in a lighter tone are used to represent the ethanol pathway, which drifts from that of ethylene upon the sixth proton-electron transfer. EtOH: ethanol.

Within the thermodynamic approach used here, the potential-limiting step (PLS) is the step with the largest positive free energy. In all four model active sites the PLS is the first proton-electron transfer. Indeed, this C-C coupling step is experimentally known to be critical in the C_2 pathway.[41,48] Concretely, 0.50, 0.52, 1.14, and 0.66 eV are the free energies of the PLS for the Cu(100), 4AD@Cu(100), Cu(111), and 4AD@Cu(111) surface models, respectively. The considerably larger value for Cu(111) is consistent with previous experiments and calculations, which showed that this facet is probably one of Cu's least active facets toward C_2 products, and usually favors CH_4 evolution.[19,20,49] Comparing the 4AD@Cu(111) model with Cu(111), we observe that undercoordination helps in lowering the free energy of the PLS by appreciably stabilizing $*C_2O_2H$, i.e. the hydrogenated *CO dimer. However, the least endothermic energies correspond to the square-symmetry slabs Cu(100) and 4AD@Cu(100), which display similar values, indicating that the presence of square sites is a more important factor for *CO dimerization than surface coordination.

Figure 3 dissects the energetics of the first electrochemical step in Figure 2 ($2CO_{(g)} + * + H^+ + e^- \rightarrow *C_2O_2H$), including a *CO dimer configuration proposed previously.[50] The kinetic barriers for the formation of the dimer ($*C_2O_2$) were calculated and found to be essentially equal to the thermodynamic energy difference between 2 *CO and $*C_2O_2$, implying a late transition state. These values are provided in the inset of Figure 3. Kinetic barriers at 0 V vs RHE of 1.52 and 1.22 eV for Cu(111) and 4AD@Cu(111), confirm that C-C coupling is not favored on hexagonal symmetry surfaces. Lower values of 0.81 and 0.91 eV are calculated for Cu(100) and 4AD@Cu(100) at that potential. Note in passing that in the formation of $*C_2O_2H$, the proton-electron transfer is known to be decoupled,[7,21,38,41] such that the electron is transferred first, and the proton transfer follows. This explains an important experimental observation of CO reduction: on Cu(100), CH_4 formation depends on the pH in the SHE scale while C_2H_4 formation does not.[7,41,51]

Moreover, this decoupled transfer implies that the activation barrier for *CO dimerization is potential-dependent and pH-independent in the SHE scale.[21] Through Bader analysis[52] we determined that, at the transition state, ~0.9 e^- have been transferred to the activated complex. Following the method described in section S8, at a potential of -0.4 V vs RHE, where C_2 species are typically reported to start evolving from Cu electrodes,[3,41,53] the dimer formation barriers are 0.45 and 0.55 eV for Cu(100) and 4AD@Cu(100). At such potential, the barriers for Cu(111) and 4AD@Cu(111) are 1.16

and 0.86 eV. Typically, surmountable barriers at room temperature are below 0.75 eV.[53] All this suggests that regarding CO-CO coupling, 4AD@Cu(100) does not feature an improvement with respect Cu(100). However, CO dimerization is favored at square symmetry sites (Cu(100) and 4AD@Cu(100)) with respect to hexagonal sites (Cu(111) and 4AD@Cu(111)) and the barriers are surmountable under experimental conditions.

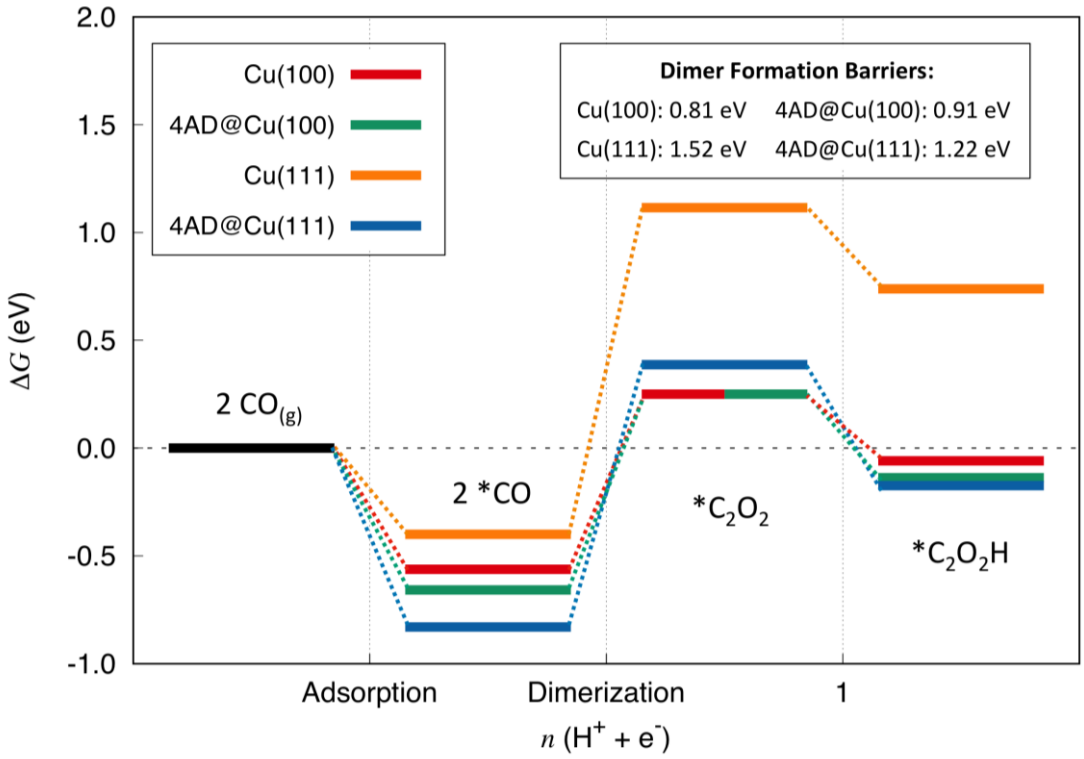

Figure 3. Free-energy diagram at 0 V vs RHE for CO dimerization at the four types of active sites under study. Color code as in Figure 1, see top left corner. Inset: *CO dimerization barriers at 0 V vs RHE for each active site. Note that the formation of $*C_2O_2$ takes place through a decoupled electron-then-proton transfer.

While CO dimerization energetics is paramount for C_1 vs C_2 selectivity, it does not influence the selectivity among C_2 products. The sixth proton-electron transfer is key in this context, as it is the step where the ethanol and ethylene pathways bifurcate. As shown in Figure 2, both hexagonal surfaces (Cu(111) and 4AD@Cu(111)) have a clear preference for ethanol formation, since after the sixth proton-electron transfer acetaldehyde is the thermodynamically more stable intermediate. However, as mentioned before, unfavorable CO dimerization prevents these surfaces from producing significant amounts of multi-carbon products, which can be mitigated by opening alternative pathways upon e.g. alloying Cu with Ag.[54,55] Conversely, Cu(100) features

favorable energetics for C-C coupling and is inclined toward ethylene formation. This leaves 4AD@Cu(100) as the only model active site able to couple two *CO at reasonably negative potentials and exhibiting a clear preference for ethanol evolution.

A closer look at the free-energy diagram of 4AD@Cu(100) in Figure 2a, reveals that the ethylene pathway requires an energy input of 0.61 eV at the sixth proton-electron transfer. This value is slightly larger than the energy needed for producing $*C_2O_2H$ from 2*CO, indicating that for those specific sites the ethylene and the ethanol pathway have different PLSs and ethylene formation likely requires a more negative onset potential than ethanol evolution. This is yet another reason to postulate this atomic configuration as a plausible atomic configuration for the ethanol-producing active sites at OD-Cu catalysts, although the main reason is explained in detail below.

Analyzing the energetics of the sixth proton-electron transfer, we observed that the ethanol vs ethylene selectivity is essentially modulated by the interplay of three factors: the adsorption energy of acetaldehyde, the stability of acetaldehyde in solution, and the *O adsorption energy. Note in passing that the adsorption energy of $*CH_2CHO$ is not a determining factor, since it is the reference for the formation of both *O + $C_2H_{4(g)}$ and CH_3CHO. In Figure 4, a closer look at the dependence of the aforementioned three factors with the surface coordination number is displayed. The step edge of Cu(211) slabs, with a coordination number of 7, is also featured in the plot for completeness and we emphasize that essentially any site with such coordination number might have been added. Adsorbed acetaldehyde values are shown in green, and *O + $C_2H_{4(g)}$ data in blue. The stability of liquid acetaldehyde is independent of the surface structure and is shown as a dotted black line at a free energy of zero, since all the data in the figure are referenced to it.

If adsorbed or liquid acetaldehyde are more stable than *O + $C_2H_{4(g)}$, the ethanol pathway is thermodynamically preferred; otherwise, ethylene evolution would be preferred. Liquid acetaldehyde is usually more stable than its adsorbed counterpart at high coordination sites, as is the case of Cu(100) and Cu(111) surfaces, with coordination numbers 8 and 9, respectively. However, undercoordinated sites bind acetaldehyde strong enough to prevent its desorption once formed, inclining the selectivity towards ethanol production. Hence, active sites that tend to bind acetaldehyde strongly, i.e. sites with coordination number 7 or lower, are good candidates for enhancing ethanol selectivity.

Furthermore, ethanol evolution will be favored when the active sites bind *O weakly. It is known that less coordinated sites at metals generally bind adsorbates more strongly than the more coordinated ones (e.g. Figure S5 for 2*CO),[56-59] but this is not forcedly the case for all metals and adsorbates. In the case of *O at Cu, as seen in Figure 4, there is no clear correlation between adsorption energies and coordination numbers. Conversely, the correlation is evident for acetaldehyde, which exhibits a good correlation coefficient. Thus, we conclude that weak *O adsorption enhances ethanol evolution, but it is difficult to predict what atomic structure is needed to fulfill this requisite. According to Figure 4, 4AD@Cu(100) sites bind *O more weakly than Cu(100), indicating that the square, four-atom islands incline the selectivity towards ethanol. In fact, *CH_3CHO is more stable than *O + C_2H_4 by 0.46 eV (see Table S3). Note in passing that this type of comparisons (*i.e.* ΔG_2 vs ΔG_1) is habitually used in computational electrocatalysis to predict/rationalize the selectivity of reactions.[60,61] In line with Lum *et al.* conclusions,[24] Figure 4 suggests that in OD-Cu catalysts in which a multiplicity of sites coexist, 4AD@Cu(100) is primarily responsible for producing ethanol, whereas other sites such as (100) terraces mainly produce ethylene.

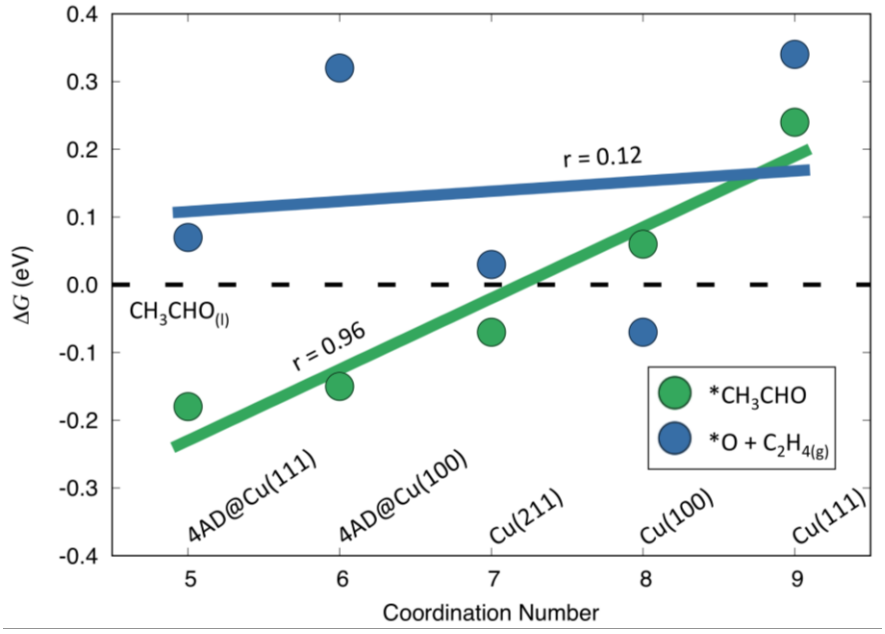

Figure 4. Free energies of adsorption of CH_3CHO (green) and *O + $C_2H_{4(g)}$ (blue) versus the coordination number of the active sites at different surface models. The linear regression for each set of values is provided together with the corresponding Pearson regression coefficient (r). The linear equations are y = -0.76 + 0.11x and y = 0.03 + 0.02x for the green and blue lines, respectively. All energies are referenced to liquid acetaldehyde (black dashed line).

Conclusions

Oxide-derived Cu catalysts are remarkably active for CORR to C_2 species. In spite of the extensive research devoted to exploit and enhance their electrocatalytic activity and selectivity, the atomic-scale nature of their active sites has not been fully identified yet. On the basis of a computational model including thermodynamic and kinetic data, solvent and cation effects, here we proposed square, four-atom islands (4AD@Cu(100)) as the active sites of OD-Cu for CORR to ethanol. These sites feature favorable *CO dimerization energetics by virtue of their square shape, and ethanol selectivity granted by their undercoordination. We ruled out active sites with hexagonal symmetry, either with large or low surface coordination numbers.

Finally, we pointed out that the relative thermodynamic stability of adsorbed and liquid acetaldehyde with respect to *O determines the CORR selectivity of the active sites towards ethylene or ethanol. Since we found no apparent correlation between *O adsorption and coordination numbers on Cu, sites with enhanced selectivity need to be engineered with great caution and using more advanced structural descriptors. We hope this all provides insightful guidelines for the design of CO and CO_2 reduction active sites with enhanced ethanol selectivity.

Associated Content

Supporting Information

The following Supporting Information is available free of charge on the ACS Publications website at DOI: details on gas-phase corrections, liquid-phase corrections, solvation contributions to the free energies, adsorption energy values, stability of the 4-atom Cu islands, cation effects, alternative pathways, CO coupling kinetics, and coordinates of the optimized systems.

Acknowledgments

This work has been supported by Spanish MICIUN's RTI2018-095460-B-I00 and María de Maeztu MDM-2017-0767 grants and, in part, by Generalitat de Catalunya 2017SGR13, XRQTC grants and by COST Action 18234, supported by COST (European Cooperation in Science and Technology). F.C.V. thanks the Spanish MICIUN for a Ramón y Cajal research contract (RYC-2015-18996) and F.I. acknowledges additional support from the 2015 ICREA Academia Award for

Excellence in University Research. O.P. thanks the Spanish MICIUN for an FPI PhD grant (PRE2018-083811). F. V. thanks the Spanish MICIUN for a Ramón y Cajal research contract (RYC-2012-10129). We are thankful to Red Española de Supercomputación (RES) for super-computing time at SCAYLE (projects QS-2019-3-0018, QS-2019-2-0023, and QCM-2019-1-0034). The use of supercomputing facilities at SURFsara was sponsored by NWO Physical Sciences. F.C.V. thanks Dr. Ioannis Katsounaros for insightful discussions. Patricia Verdugo is gratefully acknowledged for her help with the design of the TOC figure.

Table of Contents

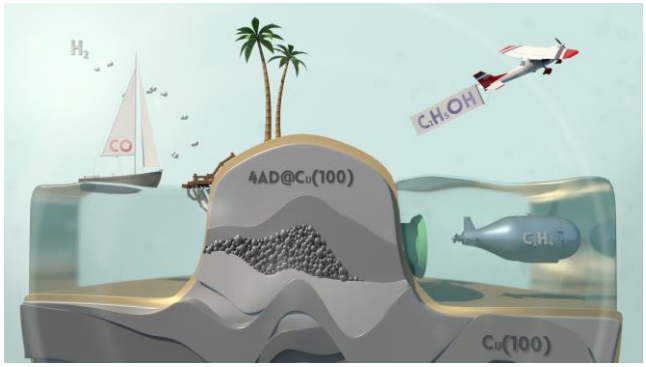

355 **References**

(1) Bushuyev, O. S.; Luna, P. D.; Dinh, C. T.; Tao, L.; Saur, G.; van de Lagemaat, J.; Kelley, S. O.; Sargent, E. H. What should we make with CO_2 and how can we make it? *Joule* **2018**, 2, 825-832.

(2) Gao, D.; Arán-Ais, R. M.; Jeon, H. S.; Cuenya, B. R. Rational catalyst and electrolyte design for CO_2 electroreduction towards multicarbon products. *Nat. Catal.* **2019**, 2, 198-210.

(3) Birdja, Y. Y.; Pérez-Gallent, E.; Figueiredo, M. C.; Göttle, A. J.; Calle-Vallejo, F.; Koper, M. T. M. Advances and challenges in understanding the electrocatalytic conversion of carbon dioxide to fuels. *Nat. Energy* **2019**, 4, 732-745.

(4) Handoko, A. D.; Wei, F.; Jenndy, Yeo, B. S.; Seh, Z. W. Understanding heterogeneous electrocatalytic carbon dioxide reduction through operando techniques. *Nat. Catal.* **2018**, 1, 922-934.

(5) Hori, Y.; Murata, A.; Takahashi, R.; Suzuki, S. Electroreduction of carbon monoxide to methane and ethylene at a copper electrode in aqueous solutions at ambient temperature and pressure. *J. Am. Chem. Soc.* **1987**, 109, 5022-5023.

(6) Hori, Y.; Murata, A.; Takahashi, R. Formation of hydrocarbons in the electrochemical reduction of carbon dioxide at a copper electrode in aqueous solution. *J. Chem. Soc. Faraday Trans. 1* **1989**, 85, 2309-2326.

(7) Hori, Y.; Takahashi, R.; Yoshinami, Y.; Murata, A. Electrochemical reduction of CO at a copper electrode. *J. Phys. Chem. B* **1997**, 101, 7075-7081.

(8) Chen, Y.; Li, C. W.; Kanan, M. W. Aqueous CO_2 reduction at very low overpotential on oxide-derived Au nanoparticles. *J. Am. Chem. Soc.* **2012**, 134, 19969-19972.

(9) Ma, M.; Trzesniewski, B. J.; Xie, J.; Smith, W. A. Selective and efficient reduction of carbon dioxide to carbon monoxide on oxide-derived nanostructured silver electrocatalysts. *Angew. Chem. Int. Ed*. **2016**, 55, 9748-9752.

(10) Li, C. W.; Kanan, M. W. CO_2 reduction at low overpotential on Cu electrodes resulting from the reduction of thick Cu_2O films. *J. Am. Chem. Soc.* **2012**, 134, 7231-7234.

(11) Li, C. W.; Ciston, J.; Kanan, M. W. Electroreduction of carbon monoxide to liquid fuel on oxide-derived nanocrystalline copper. *Nature* **2014**, 508, 504-507.

(12) Verdaguer-Casadevall, A.; Li, C. W.; Johansson, T. P.; Scott, S. B.; McKeown, J. T.; Kumar, M.; Stephens, I. E. L.; Kanan, M. W.; Chorkendorff, I. Probing the active surface sites for CO reduction on oxide-derived copper electrocatalysts. *J. Am. Chem. Soc.* **2015**, 137, 9808-9811.

(13) Eilert, A.; Cavalca, F.; Roberts, F. S.; Osterwalder, J.; Liu, C.; Favaro, M.; Crumlin, E. J.; Ogasawara, H.; Friebel, D.; Petterson, L. G. M.; Nilsson, A. Subsurface oxygen in oxide-derived copper electrocatalysts for carbon dioxide reduction. *J. Phys. Chem. Lett.* **2017**, 8, 285-290.

(14) Cavalca, F.; Ferragut, R.; Aghion, S.; Eilert, A.; Diaz-Morales, O.; Liu, C.; Koh, A. L.; Hansen, T. W.; Petterson, L. G. M.; Nilsson, A. Nature and distribution of stable

subsurface oxygen in copper electrodes during electrochemical CO_2 reduction. *J. Phys. Chem. C* **2017**, 121, 25003-25009.

(15) Liu, C; Lourenço, M. P.; Hedström, S.; Cavalca, F.; Diaz-Morales, O.; Duarte, H. A.; Nilsson, A.; Petterson, L. G. M. Stability and effects of subsurface oxygen in oxide-derived Cu catalyst for CO_2 reduction. *J. Phys. Chem. C* **2017**, 121, 25010-25017.

(16) Garza, A. J.; Bell, A. T.; Head-Gordon, M. Is subsurface oxygen necessary for the electrochemical reduction of CO_2 on copper? *J. Phys. Chem. Lett.* **2018**, 9, 601-606.

(17) Fields, M.; Hong, X.; Nørskov, J. K.; Chan, K. Role of subsurface oxygen on Cu surfaces for CO_2 electrochemical reduction. *J. Phys. Chem. C* **2018**, 122, 16209-16215.

(18) Scott, S. B.; Hogg, T. V.; Landers, A. T.; Maagaard, T.; Bertheussen, E.; Lin, J. C.; Davis, R. C.; Beeman, J. W.; Higgins, D.; Drisdell, W. S.; Hahn, C.; Mehta, A.; Seger, B.; Jaramillo, T. F.; Chorkendorff, I. Absence of oxidized phases in Cu under CO reduction conditions. *ACS Energy Lett.* **2019**, 4, 803-804.

(19) Li, H.; Li, Y.; Koper, M. T. M.; Calle-Vallejo, F. Bond-Making and Breaking between Carbon, Nitrogen, and Oxygen in Electrocatalysis. *J. Am. Chem. Soc.* **2014**, 136, 15694–15701.

(20) Hori, Y.; Takahashi, I.; Koga, O.; Hoshi, N. Electrochemical reduction of carbon dioxide at various series of copper single crystal electrodes. *J. Mol. Catal. Chem.* **2003**, 199, 39-47.

(21) Calle-Vallejo, F.; Koper, M. T. M. Theoretical considerations on the electroreduction of CO to C_2 species on Cu(100) electrodes. *Angew. Chem.* **2013**, 125, 7423-7426.

(22) Ledezma-Yanez, I.; Gallent, E. P.; Koper, M. T. M.; Calle-Vallejo, F. Structure-Sensitive Electroreduction of Acetaldehyde to Ethanol on Copper and Its Mechanistic Implications for CO and CO_2 Reduction. *Catal. Today* **2016**, 262, 90–94.

(23) Bertheussen, E.; Verdaguer-Casadevall, A.; Ravasio, D.; Montoya, J. H.; Trimarco, D. B.; Roy, C.; Meier, S.; Wendland, J.; Nørskov, J. K.; Stephens, I. E. L.; Chorkendorff, I. Acetaldehyde as an Intermediate in the Electroreduction of Carbon Monoxide to Ethanol on Oxide-Derived Copper. *Angew. Chem. Int. Ed.* **2016**, 55, 1450–1454.

(24) Lum, Y.; Ager, J. W. Evidence for Product-Specific Active Sites on Oxide-Derived Cu Catalysts for Electrochemical CO_2 Reduction. *Nat. Catal.* **2019**, 2, 86–93.

(25) Kresse, G.; Furthmüller, J. Efficient iterative schemes for *ab initio* total-energy calculations using a plane-wave basis set. *Phy. Rev. B* **1996**, 54, 11169-11186.

(26) Perdew, J. P.; Burke, K.; Ernzerhof, M. Generalized gradient approximation made simple. *Phys. Rev. Lett.* **1996**, 77, 3865-3868.

(27) Vega, L.; Ruvireta, J.; Viñes, F.; Illas, F. Jacob's ladder as sketched by Escher: assessing the performance of broadly used density functionals on transition metal surface properties. *J. Chem. Theory Comput.* **2018**, 14, 395-403.

(28) Kresse, G.; Joubert, D. From ultrasoft pseudopotentials to the projector augmented-wave method. *Phys. Rev. B* **1999**, 59, 1758-1775.

(29) Methfessel, M.; Paxton, A. T. High-precision sampling for Brillouin-zone integration in metals. *Phys. Rev. B* **1989**, 40, 3616-3621.

(30) Henkelman, G.; Uberuaga, B. P.; Jónsson, H. A climbing image nudged elastic band method for finding saddle points and minimum energy paths. *J. Chem. Phys.* **2000**, 113, 9901-9904.

(31) Lide, D. R. CRC *Handbook of Chemistry and Physics*. 85th ed, (CRC Press, 2005).

(32) He, Z.-D.; Hanselman, S.; Chen, Y.-X.; Koper, M. T. M.; Calle-Vallejo, F. Importance of solvation for the accurate prediction of oxygen reduction activities of Pt-based electrocatalysts. *J. Phys. Chem. Lett.* **2017**, 8, 2243-2246.

(33) Granda-Marulanda, L. P.; Builes, S.; Koper, M. T. M.; Calle-Vallejo, F. Influence of Van der Waals interactions on the solvation energies of adsorbates at Pt-based electrocatalysts. *ChemPhysChem* **2019**, 20, 2968-2972.

(34) Nørskov, J. K.; Rossmeisl, J.; Logadottir, A.; Lindqvist, L.; Kitchin, J. R.; Bligaard, T.; Jónsson, H. Origin of the overpotential for oxygen reduction at a fuel-cell cathode. *J. Phys. Chem. B* **2004**, 108, 17886-17892.

(35) Bagger, A.; Arnarson, L.; Hansen, M. H.; Spohr, E.; Rossmeisl, J. Electrochemical CO reduction: a property of the electrochemical interface. *J. Am. Chem. Soc.* **2019**, 141, 1506-1514.

(36) Wang, S.; Petzold, V.; Tripkovic, V.; Kleis, J.; Howalt, J. G.; Skuĺason,E.; Fernańdez, E. M.; Hvolbæk, B.; Jones, G.; Toftelund, A.; Falsig, H.; Björketun, M.; Studt, F.; Abild-Pedersen, F.; Rossmeisl, J.; Nørskov, J. K.; Bligaard, T. Universal transition state scaling relations for (de)hydrogenation over transition metals. *Phys. Chem. Chem. Phys.* **2011**, 13, 20760-20765.

(37) Wang, S.; Temel, B.; Shen, J.; Jones, G.; Grabow, L.; Studt, F.; Bligaard, T.; Abild-Pedersen, F.; Christensen, C.; Nørskov, J. Universal Brønsted-Evans-Polanyi relations for C-C, C-O, C-N, N- O, N-N, and O-O dissociation reactions. *Catal. Lett.* **2011**, 141, 370-373.

(38) Schouten, K. J. P.; Pérez-Gallent, E.; Koper, M. T. M. Structure sensitivity of the electrochemical reduction of carbon monoxide on copper single crystals. *ACS Catal.* **2013**, 3, 1292-1295.

(39) Hanselman, S; Koper, M. T. M.; Calle-Vallejo, F. Computational comparison of late transition metal (100) surfaces for the electrocatalytic reduction of CO to C_2 species. *ACS Energy Lett.* **2018**, 3, 1062-1067.

(40) Pérez-Gallent, E.; Marcandalli, G.; Figueiredo, M. C.; Calle-Vallejo, F.; Koper, M. T. M. Structure-and potential-dependent cation effects on CO reduction at copper single-crystal electrodes. *J. Am. Chem. Soc.* **2017**, 139, 16412-16419.

(41) Gattrell, M.; Gupta, N.; Co, A. A review of the aqueous electrochemical reduction of CO_2 to hydrocarbons at copper. *Journal of Electroanalytical Chemistry* **2006**, 594, 1-19.

(42) Garza, A. J.; Bell, A. T.; Head-Gordon, M. Mechanism of CO_2 reduction at copper surfaces: Pathways to C_2 products. *ACS Catal.* **2018**, 8, 1490-1499.

(43) Cheng, T.; Xiao, H.; Goddard III, W. A. Full atomistic reaction mechanism with kinetics for CO reduction on Cu(100) from ab initio molecular dynamics free-energy calculations at 298K. *Proc. Natl. Acad. Sci.* **2017**, 114, 1795-1800.

(44) Lum, Y.; Cheng, T.; Goddard, W. A.; Ager, J. W. Electrochemical CO Reduction Builds Solvent Water into Oxygenate Products. *J. Am. Chem. Soc.* **2018**, 140, 9337–9340.

(45) Clark, E. L.; Wong, J.; Garza, A. J.; Lin, Z.; Head-Gordon, M.; Bell, A. T. Explaining the Incorporation of Oxygen Derived from Solvent Water into the Oxygenated Products of CO Reduction over Cu. *J. Am. Chem. Soc.* **2019**, 141, 4191–4193.

(46) Murata, A.; Hori, Y. Product selectivity affected by cationic species in electrochemical reduction of CO_2 and CO at a Cu electrode. *Bull. Chem. Soc. Jpn.* **1991**, 64, 123-127.

(47) Singh, M. R.; Kwon, Y.; Lum, Y.; Ager, J. W.; Bell, A. T. Hydrolysis of electrolyte cations enhances the electrochemical reduction of CO_2 over Ag and Cu. *J. Am. Chem. Soc.* **2016**, 138, 13006-13012.

(48) Hori, Y.; Takahashi, R.; Yoshinami, Y.; Murata, A. Electrochemical reduction of CO at a copper electrode. *J. Phys. Chem. B* **1997**, 101, 7075-7081.

(49) Durand, W. J.; Peterson, A. A.; Studt, F.; Abild-Pedersen, F.; Nørskov, J. K. Structure effects on the energetics of the electrochemical reduction of CO_2 by copper surfaces. *Surf. Sci.* **2011**, 605, 1354-1359.

(50) Montoya, J. H.; Shi, C.; Chan, K.; Nørskov, J. K. Theoretical insights into a CO dimerization mechanism in CO_2 electroreduction. *J. Phys. Chem. Lett.* **2015**, 6, 2032-2037.

(51) Schouten, K. J. P.; Kwon, Y.; van der Ham, C. J. M.; Qin, Z.; Koper, M. T. M. A new mechanism for the selectivity to C1 and C2 species in the electrochemical reduction of carbon dioxide on copper electrodes. *Chem. Sci.* **2011**, 2, 1902-1909.

(52) Tang, W.; Sanville, E.; Henkelman, G. A grid-based Bader analysis algorithm without lattice bias. *J. Phys. Condens. Matter* **2009**, 21, 084204.

(53) Nitopi, S.; Bertheussen, E.; Scott, S. B.; Liu, X.; Engstfeld, A. K.; Horch, S.; Seger, B.; Stephens, I. E. L.; Chan, K.; Hahn, C.; Nørskov, J. K.; Jaramillo, T. F.; Chorkendorff, I. Progress and perspectives of electrochemical CO2 reduction on copper in aqueous electrolyte. *Chem. Rev.* **2019**, 119, 7610-7672.

(54) Ting, L. R. L.; Piqué, O.; Lim, S. Y.; Tanhaei, M.; Calle-Vallejo, F.; Yeo, B. S.; Enhancing CO_2 electroreduction to ethanol on copper−silver composites by opening an alternative catalytic pathway. *ACS Catal.* **2020**, 10, 4059-4069.

(55) Lee, S.; Park, G.; Lee, J. Importance of Ag−Cu biphasic boundaries for selective electrochemical reduction of CO_2 to ethanol. *ACS Catal.* **2017**, 7, 8594−8604.

(56) Jiang, T.; Mowbray, D. J.; Dobrin, S.; Falsig, H.; Hvolbæk, B.; Bligaard, T.; Nørskov, J. K. Trends in CO oxidation rates for metal nanoparticles and close-packed, stepped, and kinked surfaces. *J. Phys. Chem. C* **2009**, 113, 10548-10553.

(57) Calle-Vallejo, F.; Martínez, J. I.; García-Lastra, J. M.; Sautet, P.; Loffreda, D. Fast prediction of adsorption properties for platinum nanocatalysts with generalized coordination numbers. *Angew. Chem. Int. Ed.* **2014,** 53, 8316-8319.

(58) Calle-Vallejo, F.; Bandarenka, A. S. Enabling generalized coordination numbers to describe strain effects. *ChemSusChem* **2018**, 11, 1824-1828.

(59) Garlyyev, B.; Fichtner, J.; Piqué, O.; Schneider, O.; Bandarenka, A. S.; Calle-Vallejo, F. Revealing the nature of active sites in electrocatalysis. *Chem. Sci.* **2019**, 10, 8060-8075.

(60) Bagger, A.; Ju, W.; Varela, A. S.; Strasser, P.; Rossmeisl, J. Electrochemical CO_2 Reduction: A Classification Problem. *ChemPhysChem* **2017**, 18, 3266–3273.

(61) Johnson, L. R.; Sridhar, S.; Zhang, L.; Fredrickson, K. D.; Raman, A. S.; Jang, J.; Leach, C.; Padmanabhan, A.; Price, C. C.; Frey, N. C.; Raizada, A.; Rajaraman, V.; Saiprasad, S. A.; Tang, X.; Vojvodic, A. MXene Materials for the Electrochemical Nitrogen Reduction—Functionalized or Not? *ACS Catal.* **2020**, 10, 253–264.